ADVANCED
FUNCTIONAL
MATERIALS
www.afm-journal.de

Materials Views
www.MaterialsViews.com

Block Copolymer Packing Limits and Interfacial Reconfigurability in the Assembly of Periodic Mesoporous Organosilicas

*Andrew W. Wills, David J. Michalak, Peter Ercius, Ethan R. Rosenberg, Talita Perciano, Daniela Ushizima, Rory Runser, and Brett A. Helms**

Here poly(*N,N*-dimethylacrylamide)-*block*-poly(styrene) block copolymer micelles (BCPs) are advanced and applied to assemble periodic mesoporous organosilicas (PMOs) with noncylindrical pores. Using these BCP micelles, it is found that pore dimensions (11–23 nm), wall thicknesses (5–9 nm), and overall porosities (26%–78%) are independently programable, depending only on relative inputs for BCP and matrix former. Notably, the degree of order in all films improves as BCP loading approaches a packing limit of 63 vol%. Beyond this limit and regardless of pore dimensions, both porogen packing in the film and pore structure after thermal processing show significant deviations away from spherical close-packed lattices. The surprising absence of film collapse in this regime allows here to quantify the evolution of pore structure through the thermally driven interfacial reconfigurability of BCP micelles in the hybrid films when porogen loading exceeds the packing limit by using both scattering techniques and scanning transmission electron microscopy tomography. Finally, the PMOs here give dielectric constants of 1.2 and 1.5 above and below the BCP packing limit, respectively—the lowest ever reported for this matrix material.

1. Introduction

Controlling a material's porosity is useful in revealing and fine-tuning its properties as a dielectric, sorbent, or active layer for applications in catalysis, health, and energy.[1–16] Pores with mesoscale dimensions are of particular interest; they can be introduced by embedding molecular or polymeric porogens within the host material and then processing the composite to create mesopores.[17–28] Elucidating design rules for how mesopore dimensions, shape, spatial arrangement, and defect structure dictate properties relies on access to well-controlled, ordered architectures for a wider range of overall porosity than has been possible previously.[5,23,29,30] To advance the science of mesoscale assembly, a careful revaluation of the factors governing porogen packing and shape persistence before and after processing is needed.

We describe here a robust framework to understand the fundamental packing limits for spherical block copolymer (BCP) micellar porogens during the assembly and thermal processing of periodic mesoporous organosilicas (PMOs), shown schematically in **Figure 1**. For this work, we developed and applied a new family of block copolymer (BCP) architecture-directing agents based on a poly(styrene)-*block*-poly(*N,N*-dimethylacrylamide) (PS-*b*-PDMA) platform.[31,32] Under the acidic conditions used to hydrolyze 1,1,3,3,5,5-hexaethoxy-1,3,5-trisilacyclohexane (HETSCH), our PMO matrix precursor, we show that the HCl (*aq*) adsorbs to the corona of the PS-*b*-PDMA micelles. The electrostatic interactions that result, both between micelles, and with hydrolyzed HETSCH molecules, efficiently direct the periodic arrangements of porogens in the composite films for total porogen volume fractions spanning 26%–78%. A simple spin-on procedure was able to produce uniform films with tunable thicknesses between 50 and 1000 nm across 5 cm × 5 cm Si substrates, and controlled thermal processing yielded structurally sound PMOs for all films. Our implementation of PS-*b*-PDMA BCPs as PMO architecture-directing agents allows us to independently define a specific pore size and shape across a wide range of porosities. As such, we can provide here a more comprehensive portrait into the nonequilibrium structures and phenomena yielding PMOs than has been possible previously.[33–37]

One notable and unexpected outcome of our work includes the observation that the degree of order as determined by

Dr. A. W. Wills, Dr. P. Ercius, E. R. Rosenberg,
R. Runser, Dr. B. A. Helms
The Molecular Foundry
Lawrence Berkeley National Laboratory
Berkeley, CA 94720, USA
E-mail: bahelms@lbl.gov

Dr. D. J. Michalak
Intel Corporation
Hillsboro, OR 97124, USA

Dr. P. Ercius
The National Center for Electron Microscopy
The Molecular Foundry
Lawrence Berkeley National Laboratory
Berkeley, CA 94720, USA

Dr. T. Perciano, Dr. D. Ushizima
Computational Research Division
Lawrence Berkeley National Laboratory
Berkeley, CA 94720, USA

DOI: 10.1002/adfm.201501059

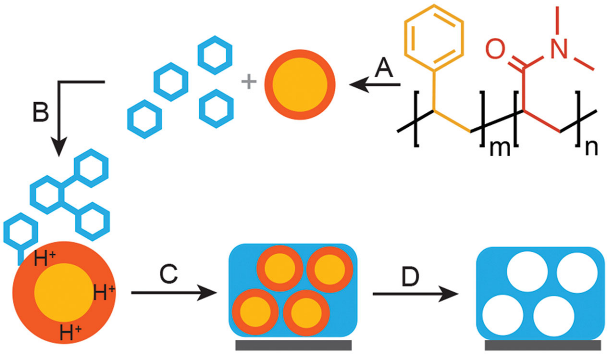

Figure 1. Assembly and thermal processing of PMOs using PS-*b*-PDMA block copolymer micelles as architecture-directing agents. A) PS-*b*-PDMA assembly into spherical micelles. B) BCP micelles are combined with PMO precursor and HCl (*aq*). C) The mixture is spin-cast onto Si substrates. Electrostatic interactions between ionized micelles direct their spatial arrangements in the composites. D) Thermal annealing vitrifies the organosilica matrix and volatilizes BCP porogens, revealing ordered uniform pores.

grazing-incidence small angle X-ray scattering (GISAXS) universally improved as porosity approached a porogen packing limit of $\approx$63 vol%, regardless of the dimensions of the micellar porogens. Body-centered-cubic (*bcc*) domains of mesopores were observable by GISAXS, as well as in the top-down scanning electron micrographs (SEM)—impressively close to the theoretical *bcc* packing limit of 68 vol% porogen. Beyond this experimentally observed packing limit, and regardless of mesopore dimensions, both porogen packing in the film and pore structure after thermal processing showed significant deviations away from simple close-packed lattices. To understand these unusual architectures, we complemented our GISAXS analysis with ellipsometric porosimetry (EP) and scanning transmission electron microscopy (STEM) tomography to characterize the coalescence of BCP porogens as their volume fraction was increased from 56% to 66%, where the critical behavior manifested. Our analysis pointed to an elongation of the initially spherical pore shapes during thermal processing when the porogen loading exceeds the 63 vol% packing limit, where the lack of matrix-forming molecules can no longer stabilize the BCP micelles. Despite this change in morphology, PMO films with overall porosities up to 78% could still be obtained, with ultra-low dielectric constants[38] (k = 1.2–1.5) consistent with our evaluation of their pore architectures.

The significance of our findings is that, using PS-*b*-PDMA BCPs as architecture-directing agents, we are able to tie PMO architectural outcomes to simple geometric packing constraints. More generally, our analysis here of the spherical BCP porogen packing limits within an organosilica matrix can be viewed alongside work in hard sphere packing, granular materials, and jammed matter. Furthermore, it suggests pathways forward for further manipulating pore architectures by diversifying the length scales (e.g., size ratios) of porogen components to achieve controllable hierarchies of pores beyond what is possible with spherical porogen packing limits.

2. Results

2.1. Design Strategy and Component Selection for Assembling Thin Films of Periodic Mesoporous Organosilicas

Our efforts to understand spherical micellar packing limits during the assembly of PMOs first required that we develop shape-persistent BCP architecture-directing agents that leverage long-range electrostatic interactions to guide the periodic arrangements of porogens in the composite films. To do so, we turned to a platform based on poly(styrene)-*block*-poly(*N*,*N*-dimethylacrylamide) (PS-*b*-PDMA) (Figure 1).[31,32] In previous work by IBM researchers, poly(D,L-lactide)-*block*-PDMA was used to generate porous organosilicas; the observed pore morphologies and phase space can vary significantly due to the dynamic character of the BCPs.[4,39] We hypothesized that exchanging the poly(D,L-lactide) block for a glassy poly(styrene) block would instead allow us to prepare more stable spherical micelles in polar solvents, and thereby allow us to realize more regular BCP packing geometries for a broader range of porogen loadings than was possible previously. We also hypothesized that a PDMA corona would be easily ionized in the presence of acid owing to the Lewis base character of the *N*,*N*-dimethylamide pendant functionality.[40] This would allow for electrostatics to efficiently guide their mesoscopic assembly in the PMO matrix upon drying of the film.

Our synthesis of PS-*b*-PDMA BCPs was carried out using reversible addition-fragmentation chain transfer (RAFT) polymerization procedures.[31,32,41,42] Three BCP architecture-directing agents were produced: PS$_{6K}$-*b*-PDMA$_{3K}$, PS$_{12K}$-*b*-PDMA$_{6K}$, and PS$_{23K}$-*b*-PDMA$_{9K}$. Micelles were generated simply by adding EtOH to molecularly-dissolved BCPs in *N*,*N*-dimethylformamide (DMF). Micelles with controllable diameters of 11, 13, and 23 nm (depending on BCP molecular weight) were demonstrated using dynamic light scattering (DLS).

For the PMO matrix precursor, we chose 1,1,3,3,5,5-hexaethoxy-1,3,5-trisilacyclohexane (HETSCH). In general, carbon-bridged organosilicas have low intrinsic dielectric constants and higher Young's moduli than terminal-methyl organosilicas.[43–46] PMOs derived specifically from HETSCH and related molecules have been explored as low-*k* dielectric interlayers.[47–51] Notably, only cylindrical pore HETSCH PMOs have been reported to date. Nonetheless, porosities up to 55% have been reported for these anisotropic PMOs, whose dielectric constants were reported as low as 1.8 for HETSCH and 1.6 for methylene-bridged compounds.[28,51,52] Higher porosities would be required to lower those values any further, if desirable. Success in that regard would ultimately require greater control over PMO assembly than has been observed previously.

2.2. Component Assembly and Thermal Processing Yielding PMO Thin Films

To gain insight into the PMO assembly process, we first characterized the interaction of PS-*b*-PDMA micelles with HETSCH matrix precursor. We first determined the diameters of the micelles by dynamic light scattering (Figure S1, Supporting Information). Upon acidification ([HCl] = 2.8 × 10^{-3} M) of a solution containing micelles but no matrix, micelle diameters increased significantly: for example, 13 nm diameter BCP micelles saw an increase in hydrodynamic diameter to 19 nm under these conditions. This increase in size is consistent with solvation and protonation of the PDMA corona. Notably, when both acid and HETSCH are added to PS-*b*-PDMA micelles in a representative sol–gel process, the micelle's hydrodynamic radius further increases to 20 nm, depending on the initial BCP:HETSCH ratio (Figure S1, Supporting Information). Our final sol–gel dispersion therefore consists of discrete, ionized, and solvated micellar porogens surrounded by one or a few molecular layers of hydrolyzed HETSCH. As these observations were nearly instantaneous and no differences were observed in films prepared from solutions aged for 10 min and 8 h, we reasoned that no ageing of the mixture was needed before attempting PMO assembly.

Assembly strategies for generating PMOs from these sol–gel dispersions should realize efficient matrix crosslinking along with clean removal of the porogen to avoid pore collapse and matrix degradation during thermal processing. After spin-casting our sol–gel dispersion onto Si substrates, we used an initial soft-bake in air at 235 ± 10 °C to densify the film. This resulted in a 15% reduction in film thickness as measured by spectral reflectance. No change in the intensity of the C—H stretching modes between 2850 and 3000 cm^{-1} was observed in the Fourier transform infrared (FTIR) spectrum before and after the soft-bake, indicating that the micellar porogens remain intact at this stage (Figure S2, Supporting Information). At the same time, a two-thirds reduction in intensity of the stretching mode at 3200 cm^{-1} was observed, indicating that densification occurred through solvent removal and silanol condensation.

We then searched for thermal annealing conditions that would volatilize the embedded BCP porogens without damaging the trisilacylohexane rings of the PMO matrix; this was done using thermogravimetric analysis (TGA) of BCP and PMO matrix degradation under isothermal conditions between 300 and 450 °C. Our data indicated that BCP porogens are efficiently removed by annealing in an inert atmosphere at, or in excess of, 400 °C (Figure S3, Supporting Information). FTIR spectroscopy of films annealed at 400 °C for 2 h showed that the trisilacylohexane rings remained intact, as evidenced by the persistence of the 1360 cm^{-1} ring vibrational mode that we identified in spectra of neat HETSCH and the shoulder on the Si–O peak below 1060 cm^{-1} (Figure S2, Supporting Information).[53] The decrease in C–H stretching intensity and total mass loss in the TGA confirmed that these processing conditions led to the removal of >95% of the BCP porogens. For films annealed at 450 °C, damage to the trisilacyclohexane ring was observed by FTIR (Figure S2, Supporting Information). Therefore, a 2 h anneal at 400 °C was selected for all further PMO processing after the initial soft-bake.

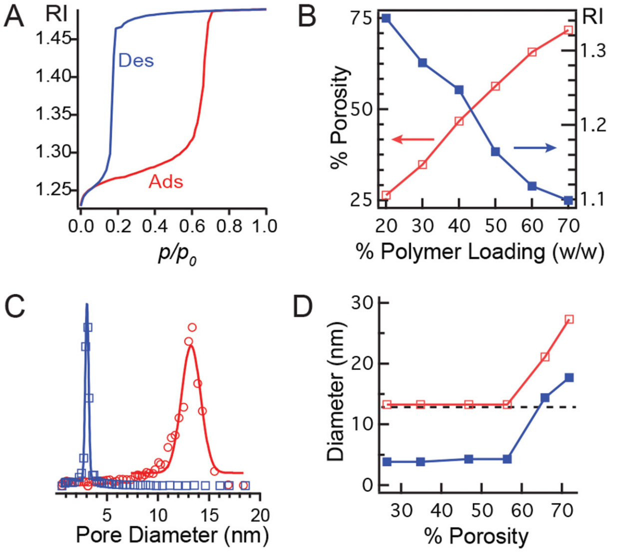

Figure 2. Ellipsometric porosimetry of annealed mesoporous films fabricated with 13 nm micelle porogen. A) Representative adsorption isotherm for refractive index (RI) versus relative pressure (p/p_0) as toluene infiltrates the film. B) The left axis shows porosity versus porogen mass loading while the right axis shows the RI of the film in air (before solvent adsorption). Mass% porogen loading is determined by (mass of porogen)/(mass of porogen + mass of matrix) and excludes solvent. C) Extracted mesopore (red) and neck (blue) diameter distribution from fits of the adsorption isotherm to the Kelvin equation. D) Mesopore and interconnecting neck diameters versus film porosity.

2.3. Identification of a Packing Limit for PS-*b*-PDMA BCP Porogens in Organosilica Matrices

With the components and processing strategy evident, we sought to investigate packing limits for spherical PS-*b*-PDMA micellar porogens when assembling HETSCH-derived PMOs. To do so, we varied the mass fraction of HETSCH matrix precursor versus PS-*b*-PDMA micelles at a fixed concentration of HCl. For all three micelle sizes, as the fraction of porogen in the mixture increased, we observed a decrease in the refractive index (RI) of the annealed films (**Figure** 2B). This correlation is a useful proxy for porosity, and allowed us to gauge whether assembly incurred any gross structural collapse during processing. Separately, we were able to quantify the total porosity in our PMO films using EP (Figure 2B).[54] As expected from RI measurements, the total porosity of the annealed films increased linearly with porogen loading; notably, we did not observe a plateau in the range of porogen loadings studied. This is in sharp contrast to porous organosilica films made with plasma enhanced chemical vapor deposition, where total porosity plateaus near 49%.[55] The well-behaved and strong dependence of porosity on porogen loading allowed us to easily tune PMO film porosity up 78%, e.g., as demonstrated for PMOs assembled with the 23 nm BCP micelles (Figures S5–S7, Table S1, Supporting Information). Furthermore, our analysis of the PMOs by EP indicated that the pore diameters of the annealed films were nearly identical to the hydrodynamic diameters of the preformed micelle porogens prior to acidification. This suggests that there is little or no intercalation of the HETSCH matrix precursor into the micelle corona during vitrification.

Given the extremes in PMO porosity available to us using these new PS-*b*-PDMA architecture-directing agents, we were interested in determining what packing arrangements of BCP porogens were present in the system throughout their loading series. We noted that for porosities below ≈26%, only isolated,

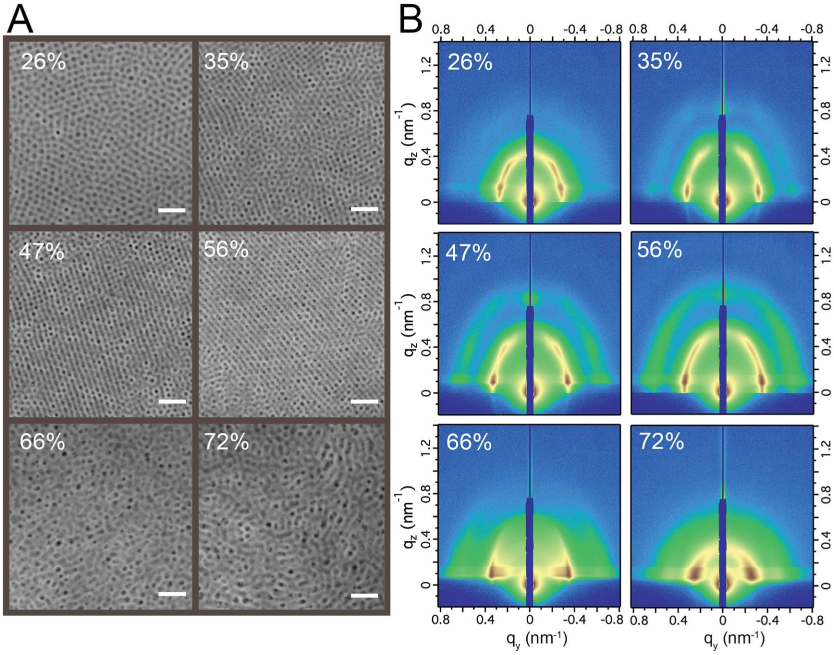

Figure 3. Evolution of pore packing and pore coalescence with increasing spherical BCP porogen loading as observed by top-down SEM (A: left panel. Scale bar is 100 nm) and GISAXS (B: right panel). Data are presented for PMOs assembled using 13 nm PS-*b*-PDMA micellar porogens. The porosity for each film was measured separately by EP (e.g., Figure 2B), and is indicated in the panels as vol%. Films were made with micelle loadings spanning 20–60 wt%. As porogen loading increases to 47–56 vol%, the films show increasing order and domain size in the SEM, while 2nd order scattering peaks become more defined in GISAXS. Grain sizes increase to several hundred nanometers (cf. Figure S8, Supporting Information, for larger area view). At 47 and 56% loading, the top-down SEM in (A) shows what appears to be a distorted 2D hexagonal pattern, which upon closer inspection shows rectangular symmetry, which could match the (110) surface of a *bcc* lattice. This was confirmed by indexing the most-intense spots in the corresponding GISAXS patterns (B). In the 47% porosity film, spots (q_y, q_z) = (0.349, 0.09), (0.24, 0.38), and (0, 0.72) were indexed to the (01–1), (101), and (022) peaks of a *bcc* unit cell with the (110) planes parallel to the substrate. Background rings indicate a distribution of grain orientations. At 66 vol% loading and beyond, close-packed order breaks down as pore coalescence is visible by SEM, while GISAXS loses all out-of-plane scattering peaks and the (01–1) smears towards lower q_y (i.e., higher periodicity).

random spherical pores were observed in the organosilica matrix by SEM; this observation was consistent for all micelle sizes. Between 26% and 63% porosity, an ordered mesoporous architecture emerged. This was evidenced in the top-down SEM (**Figure 3**A) and GISAXS (Figure 3B and Figures S4–S7, Supporting Information). GISAXS interrogates the full depth of the film across an area of ≈700 µm × 1 cm. We indexed the principal GISAXS spots for the 47%–56% porosity films in Figure 3B to a *bcc* lattice and ruled out other possible architectures.[56,57] The data collectively suggest that a minimum porogen loading is needed to reduce the distance between porogens to allow electrostatics to guide their spatial arrangements in the composite film.

For each series of PMO films assembled with a specific size of BCP porogens, a morphological distinction can be made between PMO architectures assembled with 26%–63% porosity and those with greater porosity: the former show uniform close-packed pores with the same size and shape as the micelles that templated them, while the latter exhibit elongated, disordered, and eventually worm-like pore morphologies (**Figures** 3 and **4**, and Figures S4 and S5). This abrupt increase in pore diameter and interconnectedness above 63 vol% porogen loading was readily identifiable in the EP data (Figure 2D), and was accompanied by increasingly diffuse and ever fewer scattering peaks in GISAXS (Figures 3B and 4, and Figure S6, Table S1, Supporting Information). This is clear evidence that our spherical porogens universally begin coalescing at 64% porosity.

Our observation of pore coalescence at ≈64% porosity implies that there is a porogen packing limit in our films. Related observations have been made by Stucky and Park, who found that cubic ordered mesoporous silicas could not be produced above a certain porogen:matrix stoichiometry for poly(ethylene oxide)-based BCP porogens.[23,56] We hypothesize that the order–disorder transition in our assembly scheme stems from geometric constraints on the packing of spheres during film densification. The maximum packing density for a *bcc* lattice is 68%,[58] and the porosity determined from EP is only 4% below this number. Using DLS (Figure S1, Supporting Information), we observe the adsorption of a matrix layer onto the micelles during the assembly process. We thus consider these micelle-core, matrix-shell spherical aggregates to be the primary objects undergoing packing during composite film formation. Since the films shrink during annealing and EP measures porosity post-anneal, it is likely that the density of the original core-shell aggregates corresponds to the theoretical *bcc* packing density.

2.4. Evolution of Order in PMO Architectures Through the *bcc* Porogen Packing Limit

Having identified a packing limit for PS-*b*-PDMA BCP porogens, we set out to better understand how these porogens order in the composite as a function of their volume fraction. Below the porogen packing limit, SEM revealed ordered domains of close-packed, interconnected spherical pores separated by short regions of random packing (Figure 3A). For PMOs assembled from 13 nm micelles, the (110) face of a *bcc* lattice was clearly observed. Films assembled using 11 nm micelles showed domains of a 2D hexagonally packed (2D *hex*) monolayer on top of a *bcc* lattice (Figures S4,S6, and S7, Supporting Information). It is well-known that 2D *hex* is the optimal packing density for a monolayer while *bcc* or close-packed structures are favored in the bulk, suggesting that these monolayers formed after the bulk film was assembled.[59] Finally, in the case of the 23 nm micelles, both hexagonal and cubic structures with greater

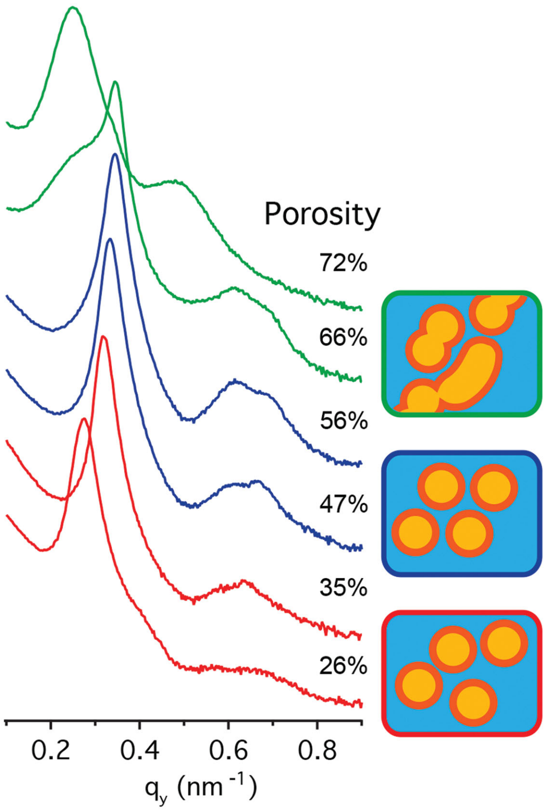

Figure 4. Line traces integrated along the q_y (in-plane) direction from GISAXS patterns taken from PMO films with varying porosity, as prepared using 13 nm PS-*b*-PDMA micelles. We note scattering peaks at $q_y = 0.34$, 0.60, and 0.68 nm^{-1} for 47% porosity. Since the primary peak has been assigned as the (01–1), the 2nd order peaks tentatively match the ratios for (21–1) and (02–2) peaks. As the porogen loading is increased from 26 to 56 vol%, the (01–1) scattering peak shifts to higher q_y, i.e., smaller periodicity. At 66% porosity, the (01–1) peak gains a low q_y shoulder due to the presence of coalesced pores. At 72% porosity, the prototypical PMO architectures observed for porosities between 26% and 56% are entirely lost.

disorder are observed by SEM and GISAXS (Figures 3 and 4, Figures S5–S7, Supporting Information).

As porosity increases from 26% to 63%, fits of the (01–1) diffraction peak reveal that the unit cell shrinks by 5–9 nm, depending on micelle size (Figure 4 and Figure S6, Table S1, Supporting Information). Pore sizes obtained from EP do not change over this range of BCP loadings (Figure 2D and Table S1, Supporting Information). Therefore, the average wall thickness must have decreased; this was confirmed by image analysis of the top-down SEM in Figure 2A. We were able to quantify the degree of uniformity in porogen packing geometry through fitting the full width at half maximum (FWHM) of the (01–1) peak obtained from GISAXS (Table S1, Supporting Information). We noted a general, monotonic decrease in FWHM as porosity was increased from 26% to 63%. This decrease correlated strongly with the grain size observed in large-area SEM images, e.g., for ≈28% versus ≈56% porosity (Figure S8, Supporting Information). In other words, pores order more uniformly and into larger grains as micelle loading approaches the 63 vol% packing limit.

We reason from these data, collectively, that the increase in porogen loading up until the packing limit results in a reduction in the degrees of freedom available to the porogen to pack within the matrix during evaporation of the solvent. At the same time, electrostatic interactions are enhanced at higher porogen loadings because the micelles are closest together, as revealed by thinner walls in the annealed structure. Electrostatics and fundamental packing relationships are therefore the primary driving forces driving the assembly outcomes for our PMOs using this unique class of BCP architecture-directing agents.

While we can precisely define the pore architectures observed below 64% porosity, the coalesced pores that form at higher porogen loadings cannot be described by simple lattices. At porosities ≥64%, the GISAXS patterns lose all signal along q_z and only show peaks along q_y (Figure 3B and Figure S6, Supporting Information). Furthermore, our assumption of spherical pores for EP characterization is invalid for these coalesced structures. We therefore turned to STEM tomography, which can provide information about both ordered and disordered domains in 3D space.[60,61] A clear pore structure can be discerned in **Figure 5** for samples taken both above and below the order–disorder transition. Shrinkage of ≈8% due to beam damage was quantified by comparing film thickness after imaging to that of the annealed film for the 58% porous sample. FFTs along the *xy* plane show periodicities of ≈15 nm, which is slightly smaller than the 19 nm nearest–neighbor spacing obtained for 11 nm micelles at this loading by GISAXS (Table S1, Supporting Information).

We were able to further assess pore packing relationships through a method called texture analysis. Texture analysis considers local variations in image intensity, which are often too fine to be distinguished as separate objects by the observer. Textural features can be statistically evaluated using the joint probability distribution of every two pixels in an image, given a direction and distance. In other words, one can calculate the gray-level co-occurrence matrix (GLCM) (Equation (1)) to consider not only the distribution of intensities, but also the spatial organization of the pixels.[62,63]

$$\begin{aligned}&P\left(I_i,I_j\,|\,\theta\right)=\pi\ \left(i,j\right)\in I_1\,|\,j=\rho\left(i,\theta\right)\}\\&\rho\left(i,\theta=0^{\circ}\right)\rightarrow\bar{x}=x+1,\bar{y}=y,\\&\rho\left(i,\theta=45^{\circ}\right)\rightarrow\bar{x}=x+1,\bar{y}=y+1,\\&\rho\left(i,\theta=90^{\circ}\right)\rightarrow\bar{x}=x,\bar{y}=y+1,\\&\rho\left(i,\theta=135^{\circ}\right)\rightarrow\bar{x}=x-1,\bar{y}=y+1\end{aligned}\tag{1}$$

Several descriptors can be extracted from the GLCM addressing contrast (i.e., the amount of local variations) and orderliness (i.e., the regularity of pixel values within an image).[64] Such descriptors differentiate between images through textural pattern change measurements. We use two descriptors derived from the GLCM: angular second moment (ASM), which describes textural homogeneity/uniformity and heterogeneity/randomness, as shown in Equations (2) and (3), respectively,

$$\mathrm{ASM}=\sum\nolimits_{i,j}P\left(I_1,I_2\right)^2\tag{2}$$

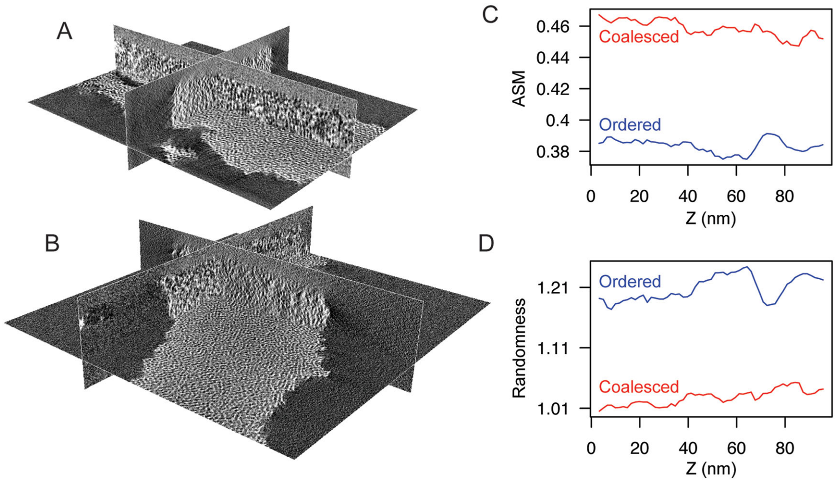

Figure 5. STEM tomography obtained on a grain of mesoporous organosilica flaked off the Si substrate after thermal processing. The films were prepared from 11 nm PS-*b*-PDMA micelles. A) A 58% porous film, and B) a 73% porous film. They were prepared from 50 to 60 wt% porogen loadings, respectively. C) and D) show the ASM and randomness GLCM functions for the STEM tomographs taken on (A) (*blue traces*) and (B) (*red traces*).

$$\text{Randomness} = -\sum_{i,j} P(I_1, I_2) \log P(I_1 I_2) \qquad (3)$$

Using textural analysis for nearest–neighbor pixels, we observe that the angular second moment is lower and randomness higher for the spherical pore (58% porous) films than the coalesced (73% porous) films (Figure 5C,D). In a porous film, the GLCM descriptors are sensitive to void–wall interfaces. High ASM and low randomness descriptors indicate more interfaces. The increase in ASM and decrease in randomness from the "Ordered" to the "Coalesced" sample indicate the disappearance of pore walls as the system goes through the order–disorder transition. Textural analysis therefore allows us to separate different pore structures in images with complex structures that are difficult for the human eye to assign and provides further confirmation of an order–disorder transition.

2.5. Evaluation of the Dielectric Constant in PMO Films At and Above the Spherical BCP Porogen Packing Limit

Having deepened our understanding of PMO assembly, we were interested providing additional metrics by which our advances might be independently corroborated and ultimately compared to results from previous work. As mentioned, PMOs have been extensively investigated for their unique properties as sorbents, supports for catalysts, and as low-*k* dielectrics.[28,65] With respect to the latter, if we were to measure the dielectric constant of our PMO films, then those might provide a convenient metric to validate our assessments of PMO architectures and compare PMO assembly approaches using different porogens as architecture directing agents, including small molecule surfactants or BCP nanostructures with different composition or morphology.

To carry out measurements of the dielectric constant for our PMO films, we modified slightly the spin-on procedure used for PMO assembly so as to obtain homogeneous film thicknesses over large substrate areas (see the Experimental Section). The PMO film impedance was measured at 100 kHz. For PMO films assembled at the spherical BCP porogen packing limit, a dielectric constant of 1.5 was obtained. To our knowledge, this is the lowest value ever reported for an ordered PMO film.[28,52] We also measured a dielectric constant of 1.2 for a disordered mesoporous film with a porosity of 79%. Our determinations of each film's dielectric constant and total porosity are consistent with predictions using the Maxwell–Garnett effective-medium approximation for HETSCH-derived porous organosilicas (**Figure 6**).

Finally, we were able to determine the hydrophobicity of our thermally processed PMO films using a technique similar to that for measuring porosity (see the Experimental Section). Depending on the context in which these PMOs might ultimately be used, dangling Si–OH bonds provide dispersed sites at the PMO surface that are available for further functionalization, e.g., using silane chemistry.[28,65] They have been also been known reduce dielectric break-down voltages and increase *k* (as water has a dielectric constant of ≈80) when PMOs served as interlayer dielectrics in integrated circuits. Quantifying hydrophobicity in these materials is thus important, and simply involves measuring total water uptake at equilibrium vapor pressure under ambient conditions.[66] For both of our films, water uptake was only 0.8%–1%; not surprisingly then, the

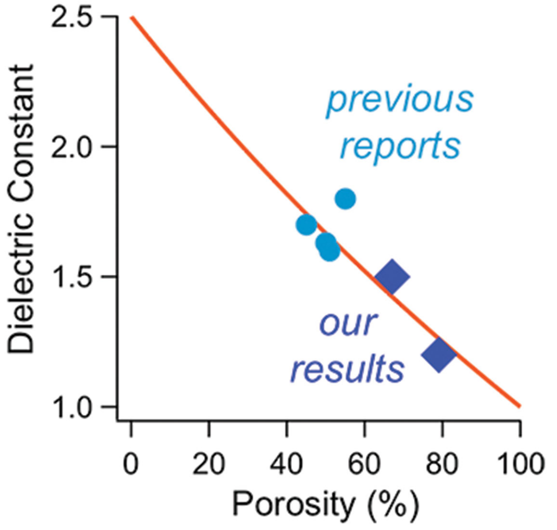

Figure 6. Theory and experiment linking dielectric properties of mesoporous organosilicas derived from HETSCH to total porosity. Prior to our work, PMO porosity had been controlled up to 55% without significant loss in order, resulting in dielectric constants of 1.6–1.8 (aqua dots).[28,52] For our PMO films, their higher porosity yielded dielectric constants of 1.5 (ordered, at the packing limit) and 1.2 (disordered, above the packing limit) (blue diamonds). Theoretical predictions of dielectric constant for a given porosity were made using the Maxwell-Garnett effective-medium approximation (red line).

dielectric breakdown voltage of both films was essentially that of air.

3. Conclusion

Fabrication of mesoporous thin films with controlled pore architectures continues to be a technological challenge that must be surmounted. Using PS-*b*-PDMA micelles as porogens, we developed a mesoporous film fabrication route that produces films with independently tunable porosity and pore size. Using the complementary techniques of SEM, GISAXS, EP, and STEM tomography we analyzed in detail the resulting pore architectures. We found that as the porogen loading is increased, porogen arrangements and ultimately pore architectures become more ordered and domain size increases, up to 63% porosity. We observe a packing limit at 63% porosity, regardless of micellar porogen dimensions, beyond which pores coalesce. By measuring the porosity of the film, we were able to tie this packing limit directly to the theoretical prediction for *bcc* packing. The ability to precisely control mesopore architecture is the first step toward elucidating definitive and meaningful mesopore structure-property relationships at multiple length and time scales.

4. Experimental Section

Materials: Styrene (99%), anisole (99.7%), and *N,N*-dimethylacrylamide (99.9%) were obtained from Sigma-Aldrich. 1,1,3,3,5,5-hexaethoxytrisilacylohexane (HETSCH) was obtained from Gelest. Reagent alcohol (EtOH) was obtained from Macron Fine Chemicals and contained 5% methanol and 5% isopropanol. DMF was obtained from Honeywell. ⟨100⟩ Si wafers were obtained from Silicon Quest and were single-sided polished except for those used for FTIR, which were double-sided polished.

Synthesis of PS-b-PDMA Block Copolymer Architecture-Directing Agents: The RAFT chain transfer agent, *S*-1-dodecyl-*S′*-(*R,R′*-dimethyl-*R″*-acetic acid) trithiocarbonate, was prepared following Shea and co-workers[41] and used to synthesize PS-*b*-PDMA copolymers. In a representative synthesis of the PDMA block, chain transfer agent (73.6 mg, 0.202 mmol), azobisisobutyronitrile (3.4 mg, 2.0×10^{-2} mmol), *N,N*-dimethylacrylamide (2.01 g, 20.3 mmol), and 1,4 dioxane (2.01 g) were dissolved in a 25 mL Schlenk tube, subjected to three freeze-pump-thaw cycles, then reacted for 60 min under static N_2 at 70 °C. The reaction mixture was diluted with 10 mL acetone and precipitated dropwise into 300 mL diethyl ether twice. Size exclusion chromatography (DMF-SEC) gave a $\bar{M}_w$ of 7000 and a polydispersity index (PDI) of 1.21. To synthesize the diblock copolymer, a PDMA macroinitiator (756 mg, 0.10 mmol, $\bar{M}_w = 7000$) and styrene (1.51 g, 14.5 mmol) were dissolved in anisole (1.51 g) and charged in a 25 mL Schlenk tube, subjected to three freeze-pump-thaw cycles, and then heated at 110 °C for 64 h under static N_2. The product was diluted with 15 mL acetone and precipitated into 300 mL hexanes twice. SEC yielded a $\bar{M}_w$ of 18 400 and PDI of 1.23. Similar procedures were used to prepare two additional PS-*b*-PDMA block copolymers. The final block copolymer architecture-directing agents employed were: $PS_{6.7K}$-*b*-$PDMA_{3.7K}$ (PDI = 1.12), $PS_{12.4K}$-*b*-$PDMA_{7K}$ (PDI = 1.23), and PS_{23K}-*b*-$PDMA_{9K}$ (PDI = 1.28).

Assembly of PS-b-PDMA Micelles: To assemble micelles, PS-*b*-PDMA (100 mg) was dissolved in DMF (70 mg), after which time EtOH (630 mg) was added dropwise over 10 min to make a 12.5 wt% BCP solution in 1:9 w/w DMF:ethanol. The hydrodynamic radius of the micelles was measured by DLS on a Malvern Zetasizer and is shown in Table S1, Supporting Information. DLS showed no aggregation for at least one week.

PMO Thin Film Assembly onto Si Substrates: HETSCH in 1:9 DMF:EtOH was dissolved to make a 12.5 wt% solution. Films were prepared by combining predetermined proportions of HETSCH and micelle solutions to make 200 mg total (Table S1, Supporting Information). Hydrochloric acid (7 µL, [HCl] = 0.10 M) was added to the stirring mixture and allowed to react for 10 min. The reaction mixture was filtered through a 0.2 µm PTFE filter directly onto clean ⟨100⟩ Si wafers. Films were spun at 3000 RPM for 60 s, with a 7 s ramp. The resulting films were soft-baked at 220 °C for 45 min on a hot-plate in air. The baked films were then annealed at 400 °C for 2 h in N_2 using a 10 °C min^{-1} ramp.

PMO Thin Film Characterization: Films were characterized by spectral reflectance taken on a Filmetrics F20 Thin Film Analyzer. Refractive indices are reported at 673 nm. FTIR was taken on a Perkin–Elmer Spectrum One using films deposited on 525 µm thick double-side polished ⟨100⟩ Si wafers. The background was referenced to a sample taken from the same wafer to reduce interference between 935 and 1220 cm^{-1} from oxygen in the film. Scanning electron micrographs were obtained on a Zeiss Ultra 55 field effect gun scanning electron microscope with 2 keV accelerating voltage and a 3.5 mm working distance. Images were obtained on the in-lens detector. TGA was obtained on a TA Instruments Q5000 under Ar with a 50 °C min^{-1} ramp to the desired temperature and held for 2 h at that temperature.

Ellipsometric Porosimetry: EP was carried out on either a Semilab P1000 or PS2000 ellipsometric porosimeter, with a 60° incident angle, using toluene as the solvent for porosity measurements and water as the solvent for hydrophobicity studies. Fits to experimental data were carried out using the associated software. The Lorentz-Lorenz equation was used to extract total porosity from the adsorption isotherm by comparing the refractive indices measured at 0.01 and 0.97 p/p_0 and the Kelvin equation to extract pore diameter from the adsorption branch and neck diameter from the desorption branch, assuming a spherical pore shape. Notably, EP obtained for PMO films assembled from 11 nm micelles and 23 nm micelles at <40 wt% loadings could not be fit by this procedure due to macroscale surface striations arising during the spin-casting procedure. Instead, porosities of these films were estimated by fitting a line to the porosities obtained for all of the PMOs assembled using 13 nm diameter micelles, as well as PMOs assembled with the 23 nm micelles where the porogen loading exceeded 40 wt%; the linear correlation observed for this collection of PMOs gave an R^2 value of 0.98 suggesting a reliable estimation was demonstrated. Estimated values for porosity for these few samples may vary from actual values by up to 5%.

GISAXS: GISAXS patterns were taken at Beamline 7.3.3 at the Advanced Light Source at Lawrence Berkeley National Laboratory, using an incident angle of 0.12°, a wavelength of 1.24 Å (10 keV), and a sample to detector distance of ≈3.8 m.[67] They were recorded on a Pilatus 1 M flat detector. Patterns for PMOs assembled with 23 nm micelles were acquired at Beamline 1–5 at Stanford Synchrotron Radiation Lightsource using an incident angle of 0.08°, a wavelength of 0.775 Å (16 keV), and a sample to detector distance of ≈3 m. They were recorded on a MarCCD detector. Horizontal line profiles were integrated using the Nika software and fit with Lorentzians to obtain the in-plane periodicity.[68]

STEM Tomography: Samples were prepared for STEM tomography by flaking a thermally processed PMO film off of the Si substrate using a razor blade, and then placing the flakes on an amorphous carbon-coated TEM grid. The images were acquired with a FEI Titan 80/300 operated in STEM mode at 200 kV with a 10° convergence semiangle, and the pixel size in each image was 1.64 nm. The 3D structure was reconstructed from a series of 87 STEM images at different tilt angles from −70° to 66°. The angular step size was set at 1° at tilts below ±50° and 2° at the higher tilt angles. Alignment and reconstruction was accomplished with the eTomo software in the IMOD tomography suite.[69] The analysis and 3D renderings were produced using the Avizo 8.1.0 software package. For texture analysis, we subtracted background fluctuations through *z* by applying digital image quantization followed by median filtering (Figure S9, Supporting Information). Image quantization is a technique that aims to compress a range of intensity values of the image to a single value, i.e., small variations on gray levels are considered to have the same intensity value. The median filtering is a nonlinear digital filtering technique that removes noise from an image while preserving fine details such as edges for example. After this process, the background of the films becomes homogeneous and the material structure is highlighted, which is essential for the texture analysis. GLCM descriptors were evaluated on the processed *z*-slices using a customized Fiji/ImageJ plugin developed in Java.

Dielectric Constant Measurements: To prepare large format films with the desired thickness for dielectric measurements, the general procedures used above were modified as follows: 200 mg of a 6.25 wt% reaction mixtures with the desired ratio of BCP micelle to HETSCH was combined with 48 μL of 0.25 N HCl. The reaction was carried out normally but spun at 500 RPM for 3 min onto 2 in. × 2 in. *p*-type ⟨100⟩ Si wafers with a maximum resistance of 0.005 Ω cm. They were annealed with the standard procedure. Film thickness was measured by ellipsometry using a modified model to account for the increase in substrate conductivity, and was 140–150 nm depending on micelle concentration. The film capacitance was measured at 100 kHz with a –10 to 10 V forward and reverse sweep, using a SSM mercury probe with a contact area between 2×10^{-2} and 2.2×10^{-2} cm^2. Exact contact areas were determined using a calibrated thermal oxide. The stage was modified with a special plate to ensure good vacuum contact for small coupons in order to ensure low backside contact resistance values.

Supporting Information

Supporting Information is available from the Wiley Online Library or from the author.

Acknowledgements

The authors thank C. Zhu and A. Hexemer for helpful discussions regarding GISAXS. Some ellipsometric porosimetry and all determinations of dielectric constant, dielectric breakdown voltage, and PMO hydrophobicity were performed at Intel Corporation (Hillsboro, OR). A. W. Wills and E. R. Rosenberg were supported by a WFO contract between Intel Corporation and B. A. Helms. E. R. Rosenberg also received partial support from the U.S. Department of Energy, Office of Science, Office of Workforce Development for Teachers and Scientists (WDTS) under the Science Undergraduate Laboratory Internship (SULI) program. Synthesis of block copolymer architecture-directing agents, PMO assembly, and aspects of PMO film characterization were carried out as part of a User Project at the Molecular Foundry, which is supported by the Office of Science, Office of Basic Energy Sciences, of the U.S. Department of Energy under Contract No. DE-AC02–05CH11231. GISAXS of PMO films assembled with the smaller BCPs was carried out at beamline 7.3.3 of the Advanced Light Source, which is supported by the Director of the Office of Science, Office of Basic Energy Sciences, of the U.S. Department of Energy under the same contract. STEM tomography was performed at the National Center for Electron Microscopy, Molecular Foundry, Lawrence Berkeley National Laboratory, which is supported by the U.S. Department of Energy also under the same contract. GISAXS of PMO films assembled with the largest BCP was carried out at beamline 1–5 at the Stanford Synchrotron Radiation Lightsource, SLAC National Accelerator Laboratory, which is supported by the U.S. Department of Energy, Office of Science, Office of Basic Energy Sciences under Contract No. DE-AC02–76SF00515. T. Perciano and D. Ushizima are supported by the Director, Office of Science, Advanced Scientific Computing Research, of the U.S. Department of Energy under Contract No. DE-AC02–05CH11231. The image analysis project is a part of the Center for Applied Mathematics for Energy Research Applications (CAMERA) at Lawrence Berkeley National Laboratory. P. Ercius and B. A. Helms are supported by the Office of Science, Office of Basic Energy Sciences, of the U.S. Department of Energy under Contract No. DE-AC02–05CH11231.

Received: March 17, 2015
Revised: April 27, 2015

[1] A. Hagfeldt, M. Grätzel, *Acc. Chem. Res.* **2000**, *33*, 269.
[2] S. Förster, T. Plantenberg, *Angew. Chem. Int. Ed.* **2002**, *41*, 688.
[3] B. Hatton, K. Landskron, W. Whitnall, D. Perovic, G. A. Ozin, *Acc. Chem. Res.* **2005**, *38*, 305.
[4] T. M. Hermans, J. Choi, B. G. G. Lohmeijer, G. Dubois, R. C. Pratt, H.-C. Kim, R. M. Waymouth, J. L. Hedrick, *Angew. Chem. Int. Ed.* **2006**, *45*, 6648.
[5] M. Etienne, A. Quach, D. Grosso, L. Nicole, C. Sanchez, A. Walcarius, *Chem. Mater.* **2007**, *19*, 844.
[6] M. Vallet-Regí, F. Balas, D. Arcos, *Angew. Chem. Int. Ed.* **2007**, *46*, 7548.
[7] C. Sanchez, C. Boissière, D. Grosso, C. Laberty, L. Nicole, *Chem. Mater.* **2008**, *20*, 682.
[8] M. Nedelcu, S. Guldin, M. C. Orilall, J. Lee, S. Hüttner, E. J. W. Crossland, S. C. Warren, C. Ducati, P. R. Laity, D. Eder, U. Wiesner, U. Steiner, H. J. Snaith, *J. Mater. Chem.* **2010**, *20*, 1261.
[9] A. Thomas, *Angew. Chem. Int. Ed.* **2010**, *49*, 8328.
[10] W. Volksen, R. D. Miller, G. Dubois, *Chem. Rev.* **2010**, *110*, 56.
[11] A. Walcarius, L. Mercier, *J. Mater. Chem.* **2010**, *20*, 4478.
[12] J. E. Lee, N. Lee, T. Kim, J. Kim, T. Hyeon, *Acc. Chem. Res.* **2011**, *44*, 893.
[13] Y.-S. Lin, N. Abadeer, K. R. Hurley, C. L. Haynes, *J. Am. Chem. Soc.* **2011**, *133*, 20444.
[14] A. Vu, Y. Qian, A. Stein, *Adv. Energy Mater.* **2012**, *2*, 1056.
[15] W. Chaikittisilp, K. Muraoka, Q. Ji, K. Ariga, Y. Yamauchi, *J. Mater. Chem. A* **2014**, *2*, 12096.
[16] M. Waki, Y. Maegawa, K. Hara, Y. Goto, S. Shirai, Y. Yamada, N. Mizoshita, T. Tani, W.-J. Chun, S. Muratsugu, M. Tada, A. Fukuoka, S. Inagaki, *J. Am. Chem. Soc.* **2014**, *136*, 4003.
[17] J. S. Beck, J. C. Vartuli, W. J. Roth, M. E. Leonowicz, C. T. Kresge, K. D. Schmitt, C. T. W. Chu, D. H. Olson, E. W. Sheppard, *J. Am. Chem. Soc.* **1992**, *114*, 10834.
[18] M. Ogawa, *Chem. Commun.* **1996**, 1149.
[19] Y. Lu, R. Ganguli, C. A. Drewien, M. T. Anderson, C. J. Brinker, W. Gong, Y. Guo, H. Soyez, B. Dunn, M. H. Huang, J. I. Zink, *Nat. Mater.* **1997**, *389*, 364.
[20] M. Templin, A. Franck, A. Du Chesne, H. Leist, Y. Zhang, R. Ulrich, V. Schädler, U. Wiesner, *Science* **1997**, *278*, 1795.
[21] M. Antonietti, B. Berton, C. Göltner, H.-P. Hentze, *Adv. Mater.* **1998**, *10*, 154.
[22] P. Yang, T. Deng, D. Zhao, P. Feng, D. Pine, B. F. Chmelka, G. M. Whitesides, G. D. Stucky, *Science* **1998**, *282*, 2244.
[23] D. Zhao, Q. Huo, J. Feng, B. F. Chmelka, G. D. Stucky, *J. Am. Chem. Soc.* **1998**, *120*, 6024.
[24] E. M. Freer, L. E. Krupp, W. D. Hinsberg, P. M. Rice, J. L. Hedrick, J. N. Cha, R. D. Miller, H.-C. Kim, *Nano Lett.* **2005**, *5*, 2014.
[25] B. Lee, Y.-H. Park, Y.-T. Hwang, W. Oh, J. Yoon, M. Ree, *Nat. Mater.* **2005**, *4*, 147.
[26] F. Hoffmann, M. Cornelius, J. Morell, M. Fröba, *Angew. Chem. Int. Ed.* **2006**, *45*, 3216.
[27] M. C. Orilall, U. Wiesner, *Chem. Soc. Rev.* **2011**, *40*, 520.
[28] P. van der Voort, D. Esquivel, E. de Canck, F. Goethals, I. van Driessche, F. J. Romero-Salguero, *Chem. Soc. Rev.* **2013**, *42*, 3913.
[29] A. P. Roberts, E. J. Garboczi, *J. Am. Ceram. Soc.* **2000**, *83*, 3041.

[30] H. Fan, C. Hartshorn, T. Buchheit, D. Tallant, R. Assink, R. Simpson, D. J. Kissel, D. J. Lacks, S. Torquato, C. J. Brinker, *Nat. Mater.* **2007**, *6*, 418.
[31] R. Buonsanti, T. E. Pick, N. Krins, T. J. Richardson, B. A. Helms, D. J. Milliron, *Nano Lett.* **2012**, *12*, 3872.
[32] T. E. Williams, C. M. Chang, E. L. Rosen, G. Garcia, E. L. Runnerstrom, B. L. Williams, B. Koo, R. Buonsanti, D. J. Milliron, B. A. Helms, *J. Mater. Chem. C* **2014**, *2*, 3328.
[33] S. Inagaki, S. Guan, Y. Fukushima, T. Ohsuna, O. Terasaki, *J. Am. Chem. Soc.* **1999**, *121*, 9611.
[34] T. Asefa, M. J. MacLachlan, N. Coombs, G. A. Ozin, *Nat. Mater.* **1999**, *402*, 867.
[35] B. J. Melde, B. T. Holland, C. F. Blanford, A. Stein, *Chem. Mater.* **1999**, *11*, 3302.
[36] M. Mandal, M. Kruk, *J. Phys. Chem. C* **2010**, *114*, 20091.
[37] M. Ikai, Y. Maegawa, Y. Goto, T. Tani, I. Shinji, *J. Mater. Chem. A* **2014**, *2*, 11857.
[38] *International Technology Roadmap for Semiconductors,* http://www.itrs.net/ **2013**.
[39] J. Choi, T. M. Hermans, B. G. G. Lohmeijer, R. C. Pratt, G. Dubois, J. Frommer, R. M. Waymouth, J. L. Hedrick, *Nano Lett.* **2006**, *6*, 1761.
[40] C. Laurence, *Lewis Basicity and Affinity Scales: Data and Measurement*, John Wiley and Sons, Chichester **2010**.
[41] J. T. Lai, D. Filla, R. Shea, *Macromolecules* **2002**, *35*, 6754.
[42] D. J. Keddie, G. Moad, E. Rizzardo, S. H. Thang, *Macromolecules* **2012**, *45*, 5321.
[43] G. Dubois, W. Volksen, T. Magbitang, R. D. Miller, D. M. Gage, R. H. Dauskardt, *Adv. Mater.* **2007**, *19*, 3989.
[44] G. Dubois, W. Volksen, T. Magbitang, M. H. Sherwood, R. D. Miller, D. M. Gage, R. H. Dauskardt, *J. Sol-Gel Sci. Technol.* **2008**, *48*, 187.
[45] Y. Matsuda, J. S. Rathore, L. V. Interrante, R. H. Dauskardt, G. Dubois, *ACS Appl. Mater. Interfaces* **2012**, *4*, 2659.
[46] Y. Matsuda, N. Kim, S. W. King, J. Bielefeld, J. F. Stebbins, R. H. Dauskardt, *ACS Appl. Mater. Interfaces* **2013**, *5*, 7950.
[47] K. Landskron, B. D. Hatton, D. D. Perovic, G. A. Ozin, *Science* **2003**, *302*, 266.
[48] K. Landskron, G. A. Ozin, *Angew. Chem. Int. Ed.* **2005**, *44*, 2107.
[49] F. Goethals, B. Meeus, A. Verberckmoes, P. van der Voort, I. van Driessche, *J. Mater. Chem.* **2010**, *20*, 1709.
[50] F. Goethals, I. Ciofi, O. Madia, K. Vanstreels, M. R. Baklanov, C. Detavernier, P. van der Voort, I. van Driessche, *J. Mater. Chem.* **2012**, *22*, 8281.
[51] F. Goethals, E. Levrau, G. Pollefeyt, M. R. Baklanov, I. Ciofi, K. Vanstreels, C. Detavernier, I. van Driessche, P. van der Voort, *J. Mater. Chem. C* **2013**, *1*, 3961.
[52] W. Wang, D. Grozea, S. Kohli, D. D. Perovic, G. A. Ozin, *ACS Nano* **2011**, *5*, 1267.
[53] A. Grill, D. A. Neumayer, *J. Appl. Phys.* **2003**, *94*, 6697.
[54] M. R. Baklanov, K. P. Mogilnikov, *Microelectron. Eng.* **2002**, *64*, 335.
[55] A. Grill, *Annu. Rev. Mater. Res.* **2009**, *39*, 49.
[56] S.-B. Jung, H.-H. Park, *Thin Solid Films* **2006**, *494*, 320.
[57] J. Zhang, Z. Luo, Z. Quan, Y. Wang, A. Kumbhar, D.-M. Smilgies, J. Fang, *Nano Lett.* **2011**, *11*, 2912.
[58] A. West, *Basic Solid State Chemistry*, John Wiley and Sons, Chichester **1999**, p. 20.
[59] E. L. Thomas, D. J. Kinning, D. B. Alward, C. S. Henkee, *Macromolecules* **1987**, *20*, 2934.
[60] P. A. Midgley, J. M. Thomas, L. Laffont, M. Weyland, R. Raja, B. F. G. Johnson, T. Khimyak, *J. Phys. Chem. B* **2004**, *108*, 4590.
[61] H. L. Xin, P. Ercius, K. J. Hughes, J. R. Engstrom, D. A. Muller, *Appl. Phys. Lett.* **2010**, *96*, 223108.
[62] R. M. Haralick, K. Shanmugam, I. Dinstein, *IEEE Trans. Syst., Man, Cybern.* **1973**, *3*, 610.
[63] R. M. Haralick, *Proc. IEEE* **1979**, *67*, 786.
[64] D. M. U. Sabino, L. da Fontoura Costa, E. G. Rizzattic, M. A. Zagoc, *Real-Time Imaging* **2004**, *10*, 205.
[65] S. S. Park, M. Santha Moorthy, C.-S. Ha, *NPG Asia Mater.* **2014**, *6*, e96.
[66] M. R. Baklanov, K. P. Mogilnikov, Q. T. Le, *Microelectron. Eng.* **2006**, *83*, 2287.
[67] A. Hexemer, W. Bras, J. Glossinger, E. Schaible, E. Gann, R. Kirian, A. MacDowell, M. Church, B. Rude, H. Padmore, *J. Phys.: Conf. Ser.* **2010**, *247*, 012007.
[68] J. Ilavsky, *J. Appl. Cryst.* **2012**, *45*, 324.
[69] J. R. Kremer, D. N. Mastronarde, J. R. McIntosh, *J. Struct. Biol.* **1996**, *116*, 71.